Featured in Physics

Second-Order Microscopic Nonlinear Optical Susceptibility in a Centrosymmetric Material: Application to Imaging Valence Electron Motion

Chance Ornelas-Skarin,[1,2,*] Tatiana Bezriadina,[3,4] Matthias Fuchs,[5] Shambhu Ghimire,[1] J. B. Hastings,[6,1]
Quynh L. Nguyen,[1] Gilberto de la Peña,[1,7] Takahiro Sato,[6,1] Sharon Shwartz,[8] Mariano Trigo,[1,7]
Diling Zhu,[6] Daria Popova-Gorelova,[3,4,9] and David A. Reis[1,7,†]

[1]*Stanford PULSE Institute, SLAC National Accelerator Laboratory,*
2575 Sand Hill Road, Menlo Park, California 94025, USA
[2]*Department of Electrical Engineering, Stanford University, Stanford, California 94305, USA*
[3]*I. Institute for Theoretical Physics and Centre for Free-Electron Laser Science,*
the University of Hamburg, Notkestrasse 9, 22607 Hamburg, Germany
[4]*The Hamburg Centre for Ultrafast Imaging (CUI), Luruper Chaussee 149, 22607 Hamburg, Germany*
[5]*Institute for Beam Physics and Technology (IBPT), Karlsruhe Institute of Technology (KIT),*
76021 Karlsruhe, Germany
[6]*Linear Coherent Light Source, SLAC National Accelerator Laboratory,*
Menlo Park, California 94025, USA
[7]*Stanford Institute for Materials and Energy Sciences, SLAC National Accelerator Laboratory,*
Menlo Park, California 94025, USA
[8]*Physics Department and Institute of Nanotechnology, Bar Ilan University, Ramat Gan 52900, Israel*
[9]*Institute of Physics, Brandenburg University of Technology Cottbus-Senftenberg,*
Erich-Weinert-Straße 1, 03046 Cottbus, Germany

We report measurements of phase-matched nonlinear x-ray and optical mixing from single-crystal silicon using subresonant 0.95 eV laser pulses and 9.5 keV hard x-ray pulses from the Linear Coherent Light Source free-electron laser. The mixing signal appears as energy and momentum sidebands to the elastic Bragg peak. It is proportional to the magnitude squared of the relevant temporal and spatial Fourier components of the optically induced microscopic charges and currents. We measure the first- and second-order sideband to the 220 Bragg peak and find that the efficiency is maximized when the applied field is along the reciprocal lattice vector. For an optical intensity of approximately 10^{12} W/cm^2, we measure peak efficiencies of 3×10^{-7} and 3×10^{-10} for the first- and second-order sideband, respectively (relative to the elastic Bragg peak). The first-order sideband is consistent with induced microscopic currents along the applied electric field and an isotropic response. The second-order sideband depends nontrivially on the optical field orientation and is consistent with an anisotropic response originating from induced charges along the bonds with C_{3v} site symmetry. The results agree well with first-principles Floquet-Bloch calculations.

Subject Areas: Atomic and Molecular Physics, Condensed Matter Physics, Optics

I. INTRODUCTION

The microscopic, atomic-scale valence electron density and its dielectric response are inextricably connected to both the static and dynamic properties of materials [1]. It plays a fundamental role in bonding and the valence

[*]Contact author: ccornela@stanford.edu
[†]Contact author: dreis@stanford.edu

excitations that result in a material's macroscopic electrical, thermal, magnetic, and optical properties. The tetrahedrally bonded group-IV semiconductors are prototypical examples of the outsized role that the valence electron density, a small fraction of the total electron density, can play in the structural stability of materials. In this case, sp^3 hybridization leads to strong covalent bonding and stability against shear deformation [2,3]. Despite the important role of the valence charge density, there is a dearth of methods for directly accessing its angstrom-scale structure and excited-state dynamics, especially in the bulk.

Nonresonant x-ray scattering is a powerful tool for imaging atomic-scale structure, as the differential elastic scattering cross section is proportional to the modulus

square of the spatial Fourier transform of the electron density [4]. Conventional nonresonant x-ray scattering experiments provide this information from the entire electron density, valence, and core. Because the valence density tends to be delocalized and makes up only a small fraction of the total electron density, it can be difficult to separate from the more localized core density. In the case of the group-IV semiconductors, the ground-state valence density can be obtained by detailed measurements of quasiforbidden Bragg peaks after removing contributions from multiple scattering and anharmonic thermal vibrations [5–8].

X-ray and optical wave mixing (XOM) corresponds to the nonlinear interaction between x-ray and optical photons mediated by the valence charge density. It was originally proposed by Freund and Levine [9] and Eisenberger and McCall [10] around 1970 and has recently received renewed attention for its potential to image valence charge motion at optical frequencies with atomic-scale spatial resolution [11–18]. In the limit that the x-ray bandwidth is small compared to the optical period, phase-matched XOM in crystals appears as energy and momentum sidebands to ordinary Bragg peaks (corresponding to nonlinear sum and difference frequency generation). In this case, the x-rays are a weak probe of the optically modulated charge density and, thus, the microscopic optical susceptibility. The intensity of the sidebands $I_G^{(n)} \propto |\rho_{\vec{G}}^{(n)}|^2$. Here, $\rho_{\vec{G}}^{(n)} = \vec{G} \cdot \chi_{\vec{G}}^{(n)} [\vec{E}]^n$ are Fourier components of the electron density $\rho(\vec{r}, t)$ corresponding to the nth harmonic of the optical frequency and $\vec{G}$th spatial Fourier component of the lattice. Similarly, $\chi_{\vec{G}}^{(n)}$ are the spatial Fourier components of the local optical susceptibility $\chi^{(n)}(\vec{r})$. Thus, measurements of the amplitude and phase of the sidebands are necessary to reconstruct the motion of the atomic-scale optically induced valence electron density within the unit cell. Since the optically induced charge density is a small fraction of the already small valence charge density, the sidebands are weak, and these measurements require high-resolution analyzers to separate the sum (or difference) frequency signal from the elastic background.

The first observation of XOM was reported more than 40 years after the original proposals [11]. In that experiment, Glover *et al.* measured the first-order sum-frequency sideband between 8 keV x-rays and 1.55 eV optical photons about the 111 Bragg peak from single-crystal diamond. The results are consistent with first-principles calculations for the induced charge density residing primarily along the tetrahedral bonds. Because of the lack of phase information, only the magnitude of the 111 spatial Fourier component of the charge density at the optical frequency could be extracted. Nonetheless, the results are a particularly notable measurement of the microscopic optical response, which is strongly affected by dielectric screening and local-field effects due to the high density and atomic-scale spatial inhomogeneities

occurring on the scale of approximately 10^{-4} of the optical wavelength [19]. As we demonstrate here, higher-order wave mixing about a suitable Bragg peak yields additional symmetry information that can help localize the valence density without the need of phasing.

In this article, we report x-ray and optical wave mixing in single-crystal silicon using monochromatic x-rays from a free-electron laser. We detect the first- and second-order sum-frequency sidebands about the 220 Bragg peak correspond to the nonlinear mixing of 9.5 keV x-ray photons with one and two 0.95 eV IR photons, respectively. Silicon has the same centrosymmetric point group as diamond and, thus, a vanishing macroscopic second-order optical susceptibility in the dipole limit. Thus, the observation of a second-order sideband in a centrosymmetric material is an indication of broken inversion symmetry at the microscopic level.

We find that the first-order sideband to the Si 220 behaves qualitatively like the first-order sideband to the diamond 111 reported by Glover *et al.* In contrast, the second-order sideband corresponding to the 220 component of the local second-order optical susceptibility scales quadratically with the infrared pump intensity as expected for a perturbative nonlinear response. The IR-laser polarization dependence for the second-order sideband is inconsistent with the induced charges merely following the optical field, unlike what is seen in the first-order sideband reported here and in Ref. [11]. This and the relatively high efficiency of the second-order sideband show that it is dominated by the local second-order dipole response, as opposed to the more general multipolar contribution.

Our results are consistent with a second-order local nonlinear optical response originating from the optically induced motion of the interstitial charges with local inversion symmetry breaking and overall reduced symmetry compared to the atomic sites. In particular, from a single measurement on (001)-cut crystal, we constrain three of the four independent 220 spatial Fourier components of the local nonlinear optical susceptibility, $\chi_{11}^{(2)}(220) + \chi_{12}^{(2)}(220) \approx \chi_{15}^{(2)}(220)$ (in Voigt notation). We further determine that $\chi_{11}^{(2)}(220) \approx 1.5\chi_{15}^{(2)}(220)$ and $\chi_{12}^{(2)}(220) \approx -0.6\chi_{15}^{(2)}(220)$ using a $(\bar{1}10)$-cut crystal. Our measurements agree well with our *ab initio* calculations for x-ray scattering from the induced charge density oscillating at twice the IR-laser frequency. We note, however, that this second-harmonic component to the induced charge does not radiate and, thus, can be observed only with an atomic scale probe such as x-ray optical mixing. Details of our formalism are given in Appendixes A–E. In Sec. II, we describe the experimental setup, followed by the procedure and results in Sec. III. We conclude in Sec. IV and give a brief outlook.

II. EXPERIMENTAL APPARATUS

The measurements were performed using the x-ray pump-probe (XPP) instrument at the Linear Coherent
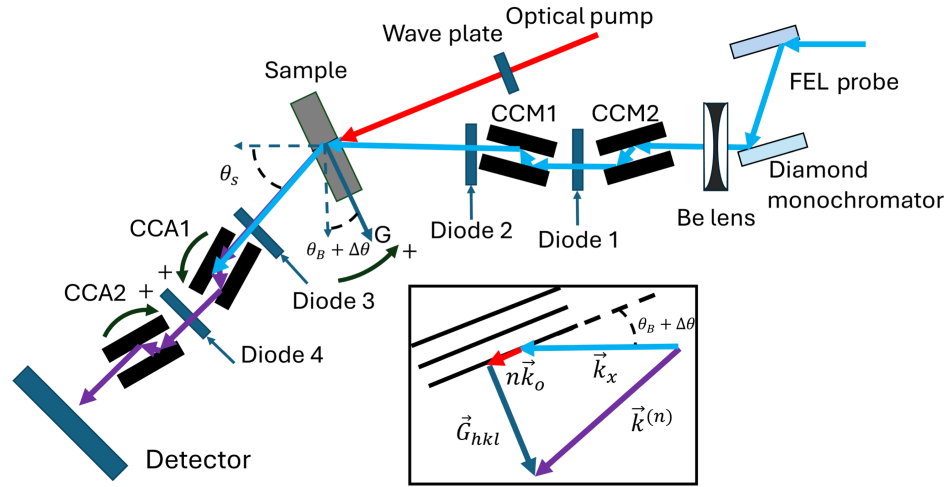
FIG. 1.   Schematic of XOM experiment setup. From the right, the FEL hard x-ray beam at 9.5 keV (shown in light blue) is monochromatized by the XPP diamond 111 large offset monochromator, before being gently focused by compound Be lenses. A secondary 311 Si channel-cut monochromator reduces the bandwidth to approximately 0.3 eV and recollimates the beam in the horizontal scattering plane. The linearly polarized 0.95 eV pump passes through a half-wave plate for varying the polarization and a lens for better matching the spot size of the x-rays. It is coupled at near normal incidence to the sample surface. The sample is 40-μm-thick (001)-cut Si. The two beams cross at the sample location, and the sample is oriented to fulfill the phase-matching conditions for producing optical sidebands to the 220 Bragg peak (shown schematically for the first-order sideband in the inset on the bottom right). In the inset, $\vec{G}_{hkl}$ is the reciprocal lattice vector ($\vec{G}_{220}$ for our measurement), $\vec{k}_x$ is the x-ray wave vector, $\vec{k}^{(n)}$ is the wave-mixing wave vector, and $n\vec{k}_o$ is the corresponding wave vector of n optical photons. Both the elastically scattered x-rays from the tail of the Bragg peak (shown in blue after the sample) and the phase-matched XOM x-rays (shown in purple after the sample) exit the crystal and enter the analyzer. The analyzer acceptance is narrow enough to allow the XOM photons onto the detector while rejecting the elastically scattered photons. Diodes 1–4 are placed along the beam path to allow real time monitoring of any drift between components.

Light Source hard x-ray free-electron laser (FEL) [20]. The FEL provided x-ray pulses at a repetition rate of 120 Hz with a central energy of 9.5 keV and a bandwidth of approximately 1 eV after the diamond 111 beam line monochromator (see Fig. 1). The x-rays are focused with a compound beryllium lens, to better match the optical spot size, and arrive at the sample position with an approximate spot size of approximately $20 \times 30 \ \mu m^2$ and a pulse length of approximately 30 fs. The x-rays are vertically polarized, and the scattering plane for both the sample and crystal optics is in the horizontal plane. The sample is a 40-μm-thick (001)-cut, float zone single-crystal silicon sample fabricated by Norcada.

After the Be lenses, the x-ray beam is further monochromated and collimated by a custom four-bounce 311 Si channel-cut monochromator (CCM1 and CCM2) in a dispersive geometry with an estimated throughput of approximately 5×10^7 photons per pulse (on average), a bandwidth of approximately 0.3 eV, and divergence ≤0.7 mdeg (12 μrad) in the horizontal plane at the sample position. The purpose of the monochromator is to create an incident x-ray beam that is sufficiently narrow in energy and divergence so that the sum-frequency signal can be well separated from the elastic background.

The sample is mounted using a manual Thorlabs RSP1 rotation mount to bring the 220 reciprocal lattice vector into the scattering plane (horizontal in the lab frame) for a symmetric Laue transmission scattering geometry. After the sample, we use a custom four-bounce 311 Si channel-cut analyzer (CCA1 and CCA2) matched to the monochromator (also in a dispersive geometry). This provides an effective filter for accepting XOM photons while rejecting the elastically scattered background photons outside this acceptance. After the analyzer, we place a pixelated Jungfrau 1M detector that measures x-rays with single-photon sensitivity on a shot-by-shot basis. Additional lead shielding is used to minimize parasitic x-ray background from air scattering and the various x-ray optics. All channel-cut crystals (CCM1, CCM2, CCA1, and CCA2) and the sample are rotated with submillidegree resolution in the scattering plane using Kohzu RA10A-W01 rotation stages.

The sample is pumped with subband gap 1300 nm (0.95 eV), approximately 100 fs, millijoule-scale pulses provided by the XPP optical parametric amplifier. The relative arrival time between each optical and x-ray pulse is given on a shot-by-shot basis using a Ce:YAG-based arrival time monitor [21]. The linearly polarized pump is focused with a 250 mm focal length lens to a measured spot size of approximately 300 μm FWHM and a peak intensity of approximately 10^{12} W/cm^2 at the sample position. We choose to couple at near normal incidence so that reflection losses from the sample are approximately independent of the polarization of the laser. The linear polarization is rotated using a half wave plate before the lens.

The x-ray flux is monitored on a shot-by-shot basis using photodiodes to measure scattered x-rays from thin Kapton films. The diodes (diodes 1–4 in Fig. 1) are placed between CCM1 and CCM2, before the sample, after the sample, and between CCA1 and CCA2 to monitor the x-ray flux between components during the measurement. The optical laser is quasirandomly mistimed with respect to the x-rays in an overall ratio of two optical laser *off* for every three optical laser *on* shots, allowing for measurement of the background under otherwise similar conditions as the signal. In the figures below, the measured data are shown with the laser-on shots (laser-off shots) as blue circles (orange circles).

III. PROCEDURE AND RESULTS

The x-ray optics and sample shown in Fig. 1 are first aligned to the elastic 220 Bragg peak (at a Bragg angle $\theta_B = 19.86°$ for our x-ray energy). After aligning the Bragg peak, the crystal is detuned according to the phase-matching condition (see Appendix E) to isolate a particular sideband and, thus, Fourier component of the induced charge density. The calculated sample detuning $\Delta\theta$ for the first- (second-) order sideband of the Si 220 peak is 20.72 (41.44) mdeg. The scattering angle and energy of the analyzer are detuned by the calculated $\Delta\theta_s = 1.9(3.8)$ mdeg and $\Delta\theta_a = 2.4(4.8)$ mdeg from the nominal conditions ($2\theta_B \approx 39.73°$ and $\theta_a \approx 23.48°$, respectively) for measuring the 220 elastic Bragg peak. Here, θ_a is the Bragg angle for the analyzers. We rotate the channel cuts to set $\Delta\theta_s$ and $\Delta\theta_a$. Since the two analyzer crystals are not mounted on a common rotation about the sample, we compensate for the change in scattering angle (and analyzer energy) by rotating them individually. This corresponds to $\Delta\theta_{CCA1} = -4.4$ (8.8) mdeg and $\Delta\theta_{CCA2} = -0.6$ (−1.2) mdeg, relative to the angles for the elastic scattering.

Once the setup in Fig. 1 is aligned, spatial and temporal overlap between the pump pulse and x-ray pulse are optimized. We assume these measurements are shot-noise limited for the purpose of the quoted errors. For all measurements, we scan only one parameter at a time, with the others nominally at their optimum value. Figures 2(a) and 2(b) show the measured dependence of the first- and second-order sideband signals, respectively, as a function of temporal delay between the x-ray and optical pulses. The temporal jitter between arrival of the x-ray and optical pulses had a FWHM of about 230 fs and was corrected using the arrival time monitor. Figure 2(a) is displayed on a logarithmic scale and shows multiple peaks due to the finite reflection of the optical beam inside the sample. The secondary peaks are spaced by the round trip time, as the phase-matching condition is met only for the nominally copropagating laser and x-ray. The peak signal for the second-order sideband is about a thousand times weaker than the first-order. In both cases, the temporal window, about 400 fs FWHM for the first-order,

for mixing is dominated by the noncollinear convolution of the two pulses that propagate with different group velocities c and c/n_g at a crossing angle of approximately θ_B.

Figures 2(c) and 2(d) show the number of detected photons per pulse as a function of $\Delta\theta$. The mdeg-scale acceptance in the elastic rocking curve [inset in Fig. 2(c)] and the first-order sideband shown in Fig. 2(c) reflect the high quality of the sample. The FWHM of the elastic Si 220 rocking curve shown in the inset in Fig. 2(c) is approximately 0.6 mdeg. We attribute the modulation in the peak shown in Fig. 2(c) to effects of the walk-off between the x-ray and optical pulse inside the crystal, which reduces the effective scattering volume compared to the unexcited scattering volume for the elastic peak. The sample detuning required to phase match in Figs. 2(c) and 2(d) matches the calculated values almost exactly. Figures 2(e) and 2(f) show the number of detected photons per pulse as a function of detuned analyzer energy ΔE, at fixed θ_s, about the first and second sideband, respectively. Figure 2(e) shows a well-defined first-order sideband on the tails of the elastic background. The peak position is approximately 1 eV above the elastic line (as expected) and has a signal to noise ratio of approximately $100:1$ and a width of 0.2 eV (expected based on the pass band of the channel-cut mono and analyzer). Similarly, the second-order sideband shows an energy shift of about 2 eV, as expected for a sum-frequency photon involving two pump photons, albeit with significantly lower statistics for the detected photons for both the on and off shots. Figures 2(g) and 2(h) show the detected photons per pulse as a function of θ_s, at fixed ΔE corresponding to the first- and second-order sideband. In both cases, the sidebands have a width of about 1 mdeg, comparable to the angular acceptance of the 311 Bragg peak.

The intensity of each sideband as a function of pump pulse energy is shown in Fig. 3. In the perturbative regime, one would expect that the first-order sideband would be linearly proportional to the laser intensity (and, thus, pulse energy) while the second-order sideband would depend quadratically. We find that the reduced χ square for a sublinear dependence (exponent of 0.683 ± 0.025 and χ square/d.o.f. of 3.228) shown in Fig. 3(a) corresponds to a much better fit than a linear fit (exponent of 1 and χ square/d.o.f. of 8.218). The second-order fits well to a nearly quadratic dependence. The deviation from the expected scaling for the first-order is significant, indicating a breakdown of perturbative scaling, although it remains unclear whether it is due to microscopic or macroscopic nonlinearities.

The measured values for the efficiency of the first- and second-order sidebands to the 220 Bragg peak are $\eta_{220}^{(1)} = 3 \times 10^{-7}$ and $\eta_{220}^{(2)} = 3 \times 10^{-10}$, respectively, relative to the (elastic) Bragg peak at the highest intensity and when the applied field is parallel to $\vec{G}$. Here, we define
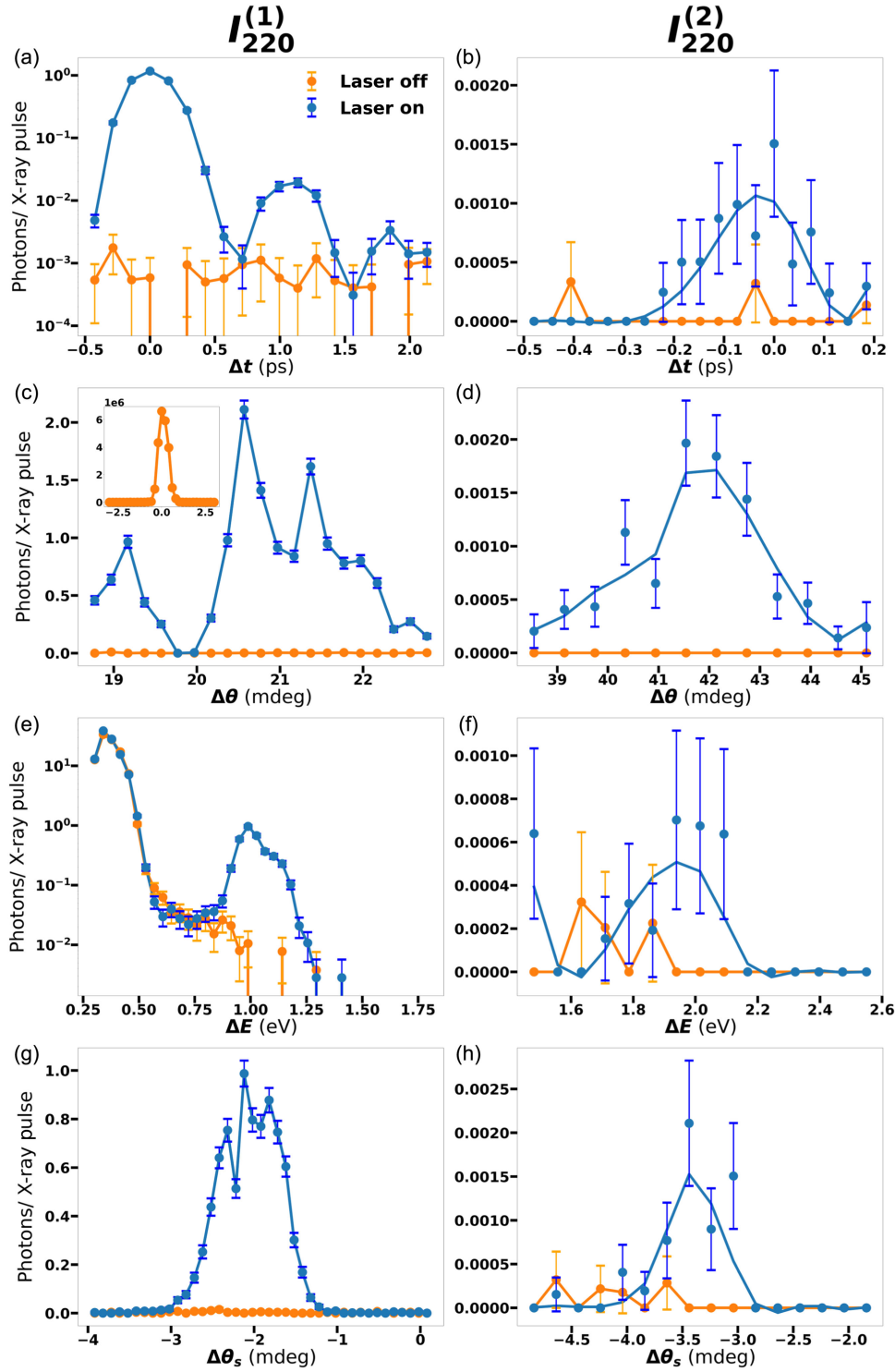
FIG. 2. Measurements of the first- (left column) and second-order (right column) XOM sidebands. Measurements with the optical laser on are shown in blue and with the optical laser off are shown in orange. XOM dependence on relative delay Δt between x-ray and optical pulse are shown for (a) first- (on a logarithmic scale) and (b) second-order sidebands. XOM dependence on sample rotation $\Delta \theta$ in the scattering plane of the (c) first- and (d) second-order sidebands. The signal is maximized when the crystal is phase matched, set to the peak of the sample rotation curve in (c) or (d), and temporal overlap is optimized, set to the peak of the relative delay curve in (a) or (b). Once the signal is maximized, the energy contents of the XOM beams measured with the analyzer are shown for the (e) first-order (on a logarithmic scale) and (f) second-order sideband. Note the tail of the elastic peak in (e) at $\Delta E \neq 0$ because the analyzer is aligned such that $\theta_s \neq 2\theta_B$. Similarly, we show the dependence of (g) the first-order sideband and (h) the second-order sideband on the scattering angle. Note that in (a) and (e) data with no counts are omitted from the plot.
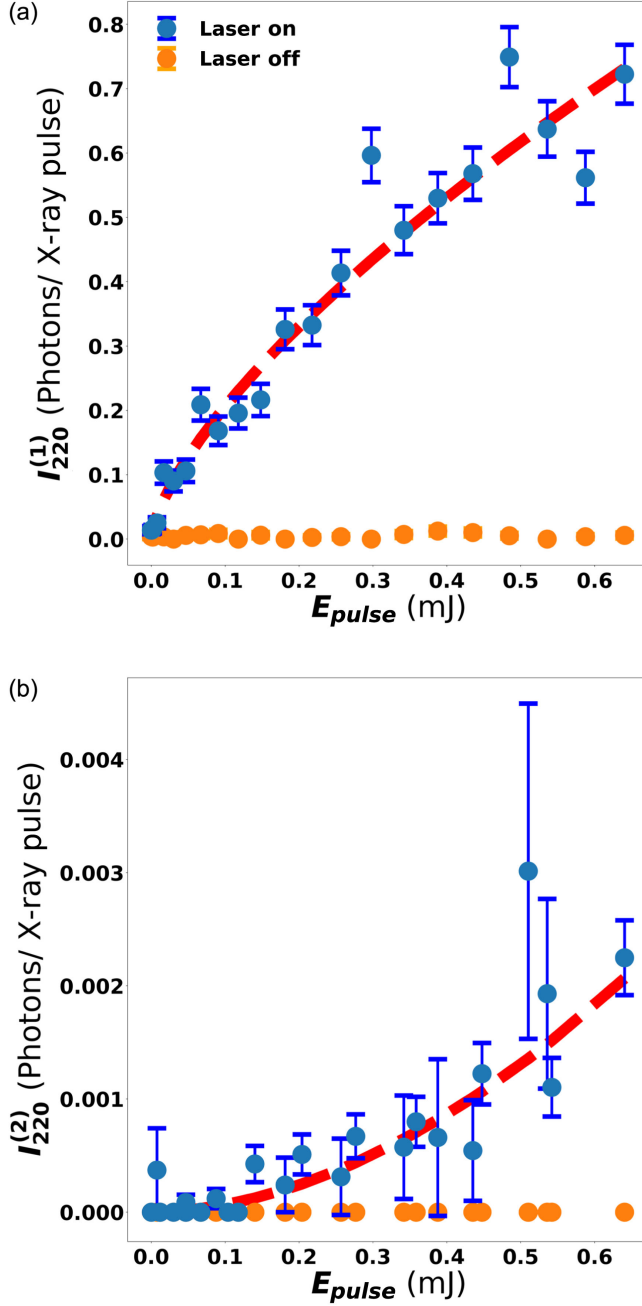
FIG. 3. (a) Optical pulse energy dependence of the first-order sideband with fit in red. (b) The optical pulse energy dependence of the second-order sideband with fit in red.

$\eta_{\vec{G}}^{(n)} \equiv I_{\vec{G}}^{(n)}/I_{\vec{G}}^{(0)}$. Because of the nature of the noncollinear wave-mixing transmission geometry, $\eta_{220}^{(1)}$ and $\eta_{220}^{(2)}$ of the sidebands will be a slight underestimate because the wave mixing scatters only from the crystal volume excited by the optical pulse, which is smaller than the crystal volume involved in the elastic scattering. We estimate a factor of 4 times less volume in the sample generating the wave-mixing photons compared to the elastically scattered photons at the Bragg peak due to walk-off

between the pump and x-ray pulses. Note that the efficiency of the second-order response is much higher than what would be expected from multipolar effects, i.e., $\eta_{220}^{(2)} \gg (\eta_{220}^{(1)})^2$. As discussed in Appendix C, this indicates that the second-order sideband is dominated by the second-order dipole response of the valence electrons which is more sensitive to local inversion symmetry breaking. This conclusion is further supported by the measurement of the polarization dependence described below.

The detected photons per pulse as a function of optical electric field direction $\vec{\epsilon}$ [rotated in the plane perpendicular to (001)] is shown for the first-order sideband in Fig. 4(a) along with the results of our *ab initio* calculations based on the Floquet-Bloch formalism [12] shown in purple (see Appendix B for details of the calculations and Appendix D). We observe a dependence proportional to the projection of the electric field along the 220 reciprocal lattice vector, which is consistent with induced motion following the field direction. This is expected for first-order sidebands of high-symmetry reciprocal lattice vectors like the 220 and is in good agreement with our theoretical calculations. Our measurement of the second-order sideband to the 220 peak as a function of the optical field direction is shown in Fig. 4(b). The second-order polarization dependence is not consistent with the induced electron motion following exactly the direction of the field. This, in addition to the efficiency of the second-order sideband, is consistent with a second-order dipole response that originates from sites in the silicon unit cell with a nonzero local microscopic $\chi^{(2)}(\vec{r}_s)$ or, in other words, where the symmetry is locally broken. The form of the polarization dependence and the sensitivity of the second-order 220 component of the optical response (see Appendix C) are consistent with the response originating at the sites between the atomic sites and the center of the bonds (with C_{3v} site symmetry). Although the atomic sites (T_d site symmetry) would be expected to also have a nonzero $\chi^{(2)}(r_s)$ individually, their contribution to the 220 component is forbidden by the symmetry of the crystal structure. The center of the bonds (the D_{3d} sites) have an identically zero $\chi^{(2)}(r_s)$, because they are centers of symmetry, and do not contribute to any spatial Fourier component for small oscillations (for more details about the sensitivity of the 220 to different site symmetries, see Appendix D).

For the (32e) C_{3v} sites, there are four independent second-order tensor components in terms of the cubic axes, (χ_{11}, χ_{12}, χ_{14}, and χ_{15}). In Appendix A, we define the reduced tensor $\Gamma_{\vec{G}}^{(n)} = \vec{G} \cdot \chi_{\vec{G}}^{(n)}$, such that $\rho_{\vec{G}}^{(n)} = \Gamma_{\vec{G}}^{(n)} \vec{E}^n$. Thus, we find that, for C_{3v} symmetry, $\rho_{220}^{(2)}$ is sensitive to three of the four tensor components (χ_{11}, χ_{12}, and χ_{15}), leading to a reduced tensor:
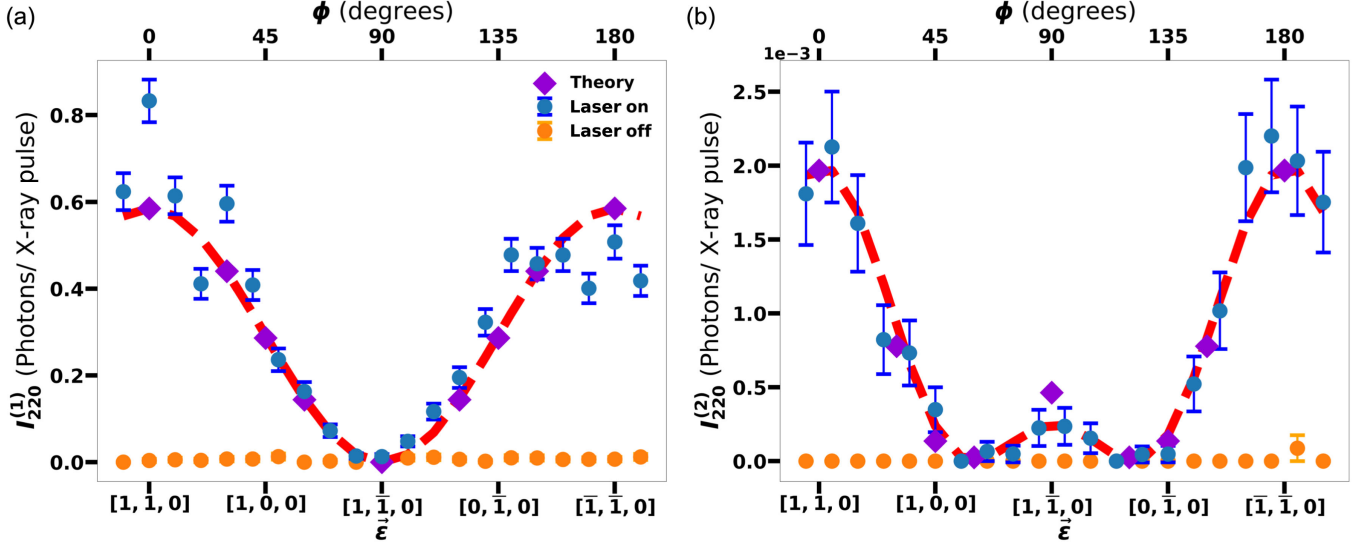
FIG. 4.   (a) The polarization dependence of the first-order sideband with phenomenological model fit results in red. (b) The polarization of the second-order sideband with phenomenological model fit results in red. Both measurements were taken with an optical field strength of approximately 10^{12} W/cm^2. For both, the relative theoretical values based on our *ab initio* calculations are shown in purple.

$$\Gamma_{220}^{(2)} = 8f_{32e}\sin 8\pi\xi \begin{pmatrix} \chi_{11}+\chi_{12} & \chi_{15} & 0 \\ \chi_{15} & \chi_{11}+\chi_{12} & 0 \\ 0 & 0 & 2\chi_{12} \end{pmatrix}, \quad (1)$$

for an effective charge of f_{32e} electrons at $\vec{r}_s = (\xi,\xi,\xi)$ and equivalent positions along the bonds (in units of the cubic lattice constant). For simplicity of notation, we drop the 220 label for these tensor components, except for where required for clarity. In our experiment on the (001)-cut crystal, the applied electric field makes an angle ϕ with respect to the 220 reciprocal lattice vector and rotates in the (001) plane. For this geometry, the expected polarization dependence of the second-order induced density

$$\rho_{220}^{(2)}(\vec{r}_{32e},\phi) \propto |\vec{E}|^2[\chi_{11}^{(2)} + \chi_{12}^{(2)} + 2\chi_{15}^{(2)}\cos(2\phi)]. \quad (2)$$

This is consistent with what we measure in Fig. 4(b). We emphasize that these results are based purely on a site symmetry analysis and, thus, require only knowledge of the space group. We constrain the values of the nonlinear tensor components by fitting Eq. (2) to our experimental results. We find that $\chi_{11}^{(2)} + \chi_{12}^{(2)} \approx \chi_{15}^{(2)}$. We perform additional measurements of the laser polarization dependence of the second-order sideband to the 220 Bragg peak in a 100-µm-thick ($\bar{1}$10)-cut crystal under similar conditions. This allows us to further constrain $\chi_{220}^{(2)}$ by rotating the electric field in a plane orthogonal to the (001) face but still containing $\vec{G} = 220$. We find that $\chi_{11}^{(2)} \approx \frac{3}{2}\chi_{15}^{(2)}$ and $\chi_{12}^{(2)} \approx -\frac{1}{2}\chi_{15}^{(2)}$. The combined results compare well with our

first-principles theoretical calculations (Appendix B) and are given in Table I.

While we have measured only two sidebands about a single Bragg peak, the very good qualitative and quantitative agreement with theory gives us confidence that our formalism will be able to predict the full excited-state density similarly well. In Fig. 5, we show the predicted first- and second-order induced density in both real [Figs. 5(a) and 5(c)] and reciprocal space [Figs. 5(b) and 5(d)] (for the {200}, {111}, {220} family of planes) for a representative set of applied electric field directions in the (001) plane and at a fixed field strength of 5×10^{11} W/cm^2. For the reciprocal space plots, the amplitude is encoded in the size of the spheres, and the color is used to encode the different families of planes. The real space density is limited to the valence density and appears primarily off the atomic sites (this is to be expected, since our first-principles calculations are based on the pseudopotential method and include only the top four valence bands originating from $3s$ and $3p$ electrons). The first-order density largely follows the field as seen in our measurements. Note that the applied field breaks the cubic symmetry of the crystal (dynamically), such that different Fourier components from the same family are, in general, no longer equivalent. Moreover, while the first-order response in

TABLE I.   Extracted components of $\chi_{220}^{(2)}$ in units of $\chi_{15}^{(2)}$.

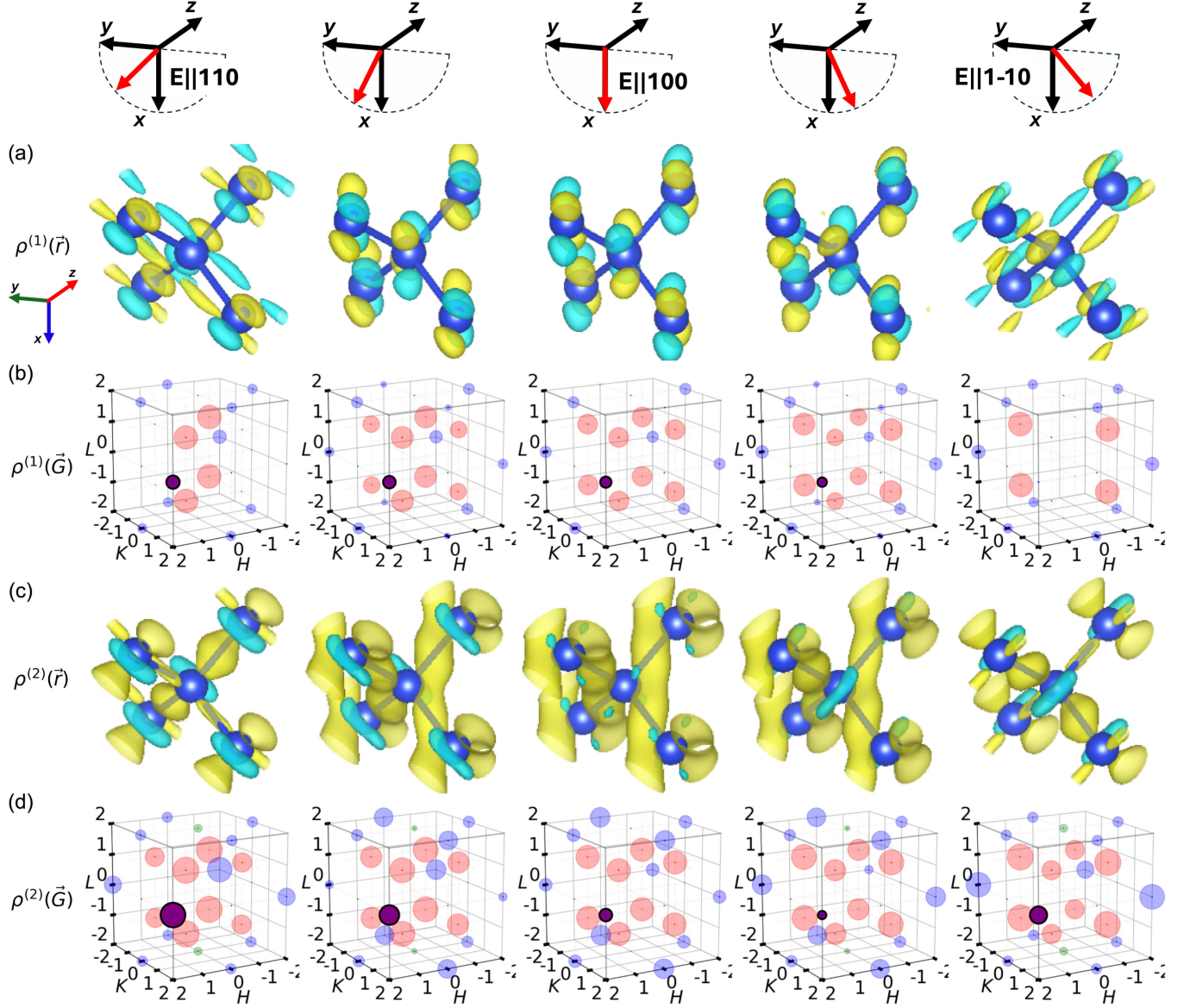|	Measurement	Theory
$\chi_{11}^{(2)} + \chi_{12}^{(2)}$	0.97 ± 0.22	0.7
$\chi_{11}^{(2)}$	1.53 ± 0.19	1.5
$\chi_{12}^{(2)}$	-0.56 ± 0.13	-0.83

FIG. 5.   *Ab initio* calculations of the induced charge densities for the first-order optical response as a function of electric field direction (with the electric field shown in red rotating within the 001 plane) in (a) real space and (b) reciprocal space. Corresponding *ab initio* calculations for induced charge densities of the second-order response in (c) real space and (d) reciprocal space. Note that in the reciprocal space plots the red spheres correspond to points in the 111 family, the blue spheres the 220 family, and the green spheres the 200 family. The points corresponding to the 220 component in the reciprocal space plots are highlighted in purple. The size of the spheres is associated with the amplitude of that component of the charge density at the given electric field direction. The isosurfaces in (a) and (c) are visualized using VESTA [22]. The yellow and blue colors represent negative and positive charges, respectively.

real space is rather complicated, $\rho^{(1)}_{\{111\}}$ and $\rho^{(1)}_{\{220\}}$ are proportional to $(\vec{G} \cdot \vec{E})^2$. The second-order response is even more nontrivial and clearly not proportional to $(\vec{G} \cdot \vec{E})^4$, as in the experimental case for the 220. In addition, we see that $\rho^{(2)}_{002}$ is allowed for $\vec{E}$ having a component along both $\hat{x}$ and $\hat{y}$ directions. This suggests that the field breaks the glide plane symmetry, which ordinarily is responsible for the strong-forbidden nature of the $\{00l\}$ family of planes when $l = 4m - 2$.

IV. CONCLUSIONS AND FUTURE DIRECTIONS

We have reported measurements of x-ray and optical wave mixing in silicon excited by below band gap optical photons. We have used phase matching and crystal optics to extract the weak nonlinear sum-frequency signals corresponding to mixing of single x-ray photons with one and two optical photons in single-crystal silicon. In principle, atomic-scale movies of the electron motion within the unit cell could be constructed by measuring multiple sidebands to multiple Bragg peaks and determining their relative

phase (for example, using maximum entropy methods [23] or multibeam diffraction [24]). Nonetheless, we have shown here that the polarization dependence of a single second-order sideband contains sufficient information to state that the second-order response is dominated by dipole effects allowed by local inversion symmetry breaking with negligible contribution from higher-order multipoles. Furthermore, we are able to attribute the second-order dipole response to particular noncentrosymmetric high-symmetry (C_{3v}) sites along the sp^3 bonds within a phenomenological point-dipole model (see Appendix C) and without direct phase information. We were also able to determine three of the four symmetry equivalent Fourier components of the local second-order optical susceptibility tensor, constrained by the particular Bragg peak. The results agree well with first-principles, Floquet-Bloch calculations for the optically excited valence electron density. These findings have important implications for understanding electronic structure and dynamics in both near-equilibrium and strongly driven materials. For example, XOM may help elucidate the microscopic mechanism underlying high harmonic generation in strongly driven solids [25] or how light-induced changes in electronic structure lead to novel functionality in quantum materials [26].

New methods are required to move beyond perfect crystals (allowing this measurement in a much wider range of materials) and ideally to perform the measurements using time-domain scattering with newly available attosecond hard x-ray pulses [27–29]. Recent advances in high-brightness fourth-generation synchrotron sources suggest that imaging valence electron motion may soon be feasible without the need for free-electron lasers.

DATA AVAILABILITY

The data that support the findings of this article are not publicly available upon publication because it is not technically feasible and/or the cost of preparing, depositing, and hosting the data would be prohibitive within the terms of this research project. The data are available from the authors upon reasonable request.

APPENDIX A: OPTICALLY INDUCED CHARGE DENSITY

In the presence of the optical field, we define the total microscopic electron density $\rho(\vec{r}, t) = \rho_0(\vec{r}) + \Delta\rho(\vec{r}, t)$. Here, $\rho_0(\vec{r})$ is the field-free density (valence and core) that is periodic in space $\rho_0(\vec{r} + \vec{R}) = \rho_0(\vec{r})$ for all lattice vectors $\vec{R}$, and $\Delta\rho(\vec{r}, t)$ is the time-dependent charge (valence) density induced by the low-frequency optical (IR) electric field $\vec{E}(\vec{r}, t)$ in the presence of screening and local-field effects.

For simplicity, we approximate the applied optical field as a monochromatic plane wave with period T_o and angular frequency $\omega_o = 2\pi/T_o$. The charge density induced by the optical field corresponds to an incommensurate and traveling charge density wave. Thus, $\Delta\rho(\vec{r}, t) = \Delta\rho(\vec{r} + \vec{R}, t + T_o)$ up to a relatively slowly varying phase factor. We expand the total charge density in terms of its Fourier components:

$$\rho(\vec{r}, t) = \sum_{\vec{G}, n} \rho(\vec{G} + n\vec{k}_o, n\omega_o) e^{-i[(\vec{G} + n\vec{k}_o)\cdot\vec{r} - n\omega_o t]}, \quad \text{(A1)}$$

where $\vec{G}$ are the reciprocal lattice vectors, n are harmonics of the optical frequency, and $k_o = 2\pi n_o/\lambda_o$ is the wave vector of the optical pump with vacuum wavelength λ_o and index of refraction n_o. For simplicity of notation, we define $\rho_{\vec{G}}^{(n)} \equiv \rho(\vec{G} + n\vec{k}_o, n\omega_o) \approx \rho(\vec{G}, n\omega_o)$, since λ_o is long compared to the lattice spacing.

We define the reduced tensor $\Gamma^{(n)}(\vec{r}) = \nabla \cdot \chi^{(n)}(\vec{r})$, in terms of a local nonlinear optical susceptibility $\chi^{(n)}(\vec{r})$, such that

$$\rho^{(n)}(\vec{r}) = \Gamma^{(n)}(\vec{r}) \cdot [\vec{E}]^n. \quad \text{(A2)}$$

Thus, the reduced tensor relates the induced charge density oscillating at the harmonics of the optical excitation for a given field magnitude and direction.

APPENDIX B: *AB INITIO* CALCULATIONS FOR SILICON

We perform *ab initio* calculations of the induced charge density $\rho^{(n)}(\vec{r})$ for optically excited silicon within the Floquet-Bloch formalism [30].

We consider a driving field with a photon energy of 0.95 eV and an intensity of 5×10^{11} W/cm². The calculations are performed using four valence bands and 76 conduction bands on a four-times shifted $12 \times 12 \times 12$ Monkhorst-Pack **k**-point grid. The infinite Floquet-Bloch Hamiltonian is approximated by a matrix with 301 blocks, each containing 80 states. The **k**-point grid, the number of bands, and the blocks are selected based on a convergence study. We apply the scissors approximation [31] to correct the direct band gap from the calculated 2.5 eV to the experimental value of 3.5 eV [32,33]. From these calculations (as a function of field direction), we determine the various components of the reduced tensor $\Gamma^{(n)}(\vec{r})$, defined in Appendix A.

In Fig. 6, we show the results of our calculations of $\Gamma^{(n)}(\vec{r})$ for the components of (a) the ground-state valence density ($n = 0$), (b) its first-order response ($n = 1$), and (c) its second-order response ($n = 2$). Note that, while $\Gamma^{(0)}(\vec{r})$ represents the ground-state density, the core-electron density

(a) $\Gamma^{(0)}(\vec{r})$

(b) $\Gamma^{(1)}(\vec{r})$

　　x　　　　y　　　　z

(c) $\Gamma^{(2)}(\vec{r})$

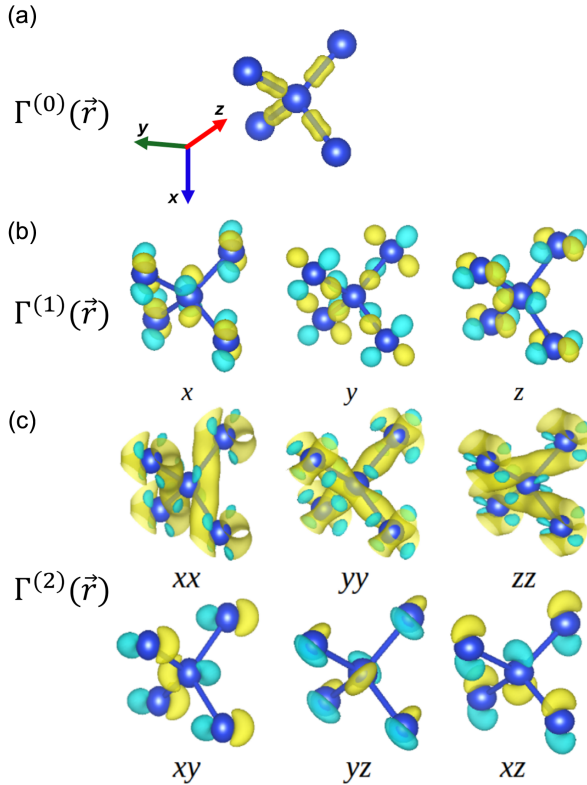　　xx　　　yy　　　zz

　　xy　　　yz　　　xz

FIG. 6.　*Ab initio* calculations of the reduced tensor components of the valence density in real space for (a) the zeroth-, (b) the first-, and (c) the second-order response to the optical field. Calculations performed for an optical intensity of 5×10^{11} W/cm².

is excluded, since we consider only the highest four conduction bands. Thus, $\Gamma^{(0)}(\vec{r})$ is distributed about the center of the bonds, as expected for sp^3 bonding.

The first-order reduced tensor components $\Gamma_i^{(1)}(\vec{r})$, where $i = x, y, z$, is distributed about the tetrahedral sites, while the second-order reduced tensor components $\Gamma_{ij}^{(2)}(\vec{r})$ show a more complex second-order density shift off the center of the bond toward the atomic sites but not onto the atomic sites. We note that the measurement of the second-order response is consistent with optically induced valence density in the space between the atomic sites and the center of the bonds.

In the experiments, we measure individual spatial and temporal Fourier components of the induced density. These can be predicted from the spatial Fourier components of $\Gamma^{(n)}(\vec{r})$:

$$\Gamma_{\vec{G}}^{(n)} = \vec{G} \cdot \chi_{\vec{G}}^{(n)}, \tag{B1}$$

where $\chi_{\vec{G}}^{(n)}$ are the spatial Fourier components of $\chi^{(n)}(\vec{r})$. Thus, the Fourier components of the charge density

$$\rho_{\vec{G}}^{(n)} = \Gamma_{\vec{G}}^{(n)} \cdot [\vec{E}]^n. \tag{B2}$$

We note that with this definition the ground-state charge density is defined as $\rho^{(0)}(\vec{r}) = \Gamma^{(0)}(\vec{r}) \equiv \nabla \cdot E_{\mathrm{loc}}(\vec{r})$, where $E_{\mathrm{loc}}(\vec{r})$ is the local field inside the crystal (in the absence of any external perturbation). In Sec. III, we present results for the first- and second-order induced density in both real and reciprocal space (for the $\{200\}, \{111\}, \{220\}$ family of planes) for a representative set of applied electric field directions sampled in the experiment and at fixed magnitude.

In the kinematic limit [34], the intensity of a sideband to a reciprocal lattice vector $\vec{G}$ is

$$I_{\vec{G}}^{(n)} \propto |\rho_{\vec{G}}^{(n)}|^2 = |\Gamma_{\vec{G}}^{(2)} \cdot [\vec{E}]^n|^2. \tag{B3}$$

We define the efficiency of a given sideband relative to the elastic Bragg peak:

$$\eta_{\vec{G}}^{(n)} = \frac{I_{\vec{G}}^{(n)}}{I_{\vec{G}}^{(0)}}. \tag{B4}$$

Thus, up to macroscopic propagation effects including walk-off, $\eta_{\vec{G}}^{(n)} = \left(\rho_{\vec{G}}^{(n)} / \rho_{\vec{G}}^{(0)} \right)^2$.

APPENDIX C: POINT-DIPOLE MODEL

We present a phenomenological point-dipole model of the optically induced charge density. We use this minimal model both to provide an intuitive interpretation of the

measurements based on symmetry and facilitate the connection between our measurements and our *ab initio* calculations. In this model, we approximate the time-varying charge density, analogous to the independent atom approximation, as

$$\rho(\vec{r}, t) = \sum_s f_s \delta[\vec{r} - \vec{r}_s - \vec{u}_s(t)], \qquad (C1)$$

where f_s is the electron density at site s and $\vec{u}_s(t) = \sum_n u_s^{(n)} \exp(in\omega_o t)$ is the induced displacement about its equilibrium position $\vec{r}_s$, oscillating at harmonics of the drive frequency. Thus,

$$\rho_{\vec{G}}^{(n)} = \frac{1}{T_o V} \int dt e^{i\omega t} \sum_s f_s e^{i\vec{G}\cdot\vec{r}_s} e^{i\vec{G}\cdot\vec{u}_s(t)}, \qquad (C2)$$

where V is the unit cell volume. Note that, even if $\vec{u}(t)$ oscillates only at the fundamental ω_0, the Fourier components of the induced density will still contain both the even and odd harmonics, since the displacements appear in the exponential. For example, in this case, $\rho^{(2)} \approx \frac{1}{2}(\rho^{(1)})^2$. In the experiments, we find that $\rho_{220}^{(2)} \gg (\rho^{(1)})^2$ and has a very different polarization dependence. Thus, $u_{220}^{(2)} \neq 0$, and the leading-order nonlinear response can be approximated as a local nonlinear dipole, $\vec{p}_s^{(n)} = -f_s \vec{u}_s^{(n)}$. In analogy with macroscopic nonlinear optics, we expand the dipole moments for site s as

$$\vec{p}_s^{(n)} = \chi^{(n)}(\vec{r}_s)[\vec{E}]^n. \qquad (C3)$$

We note that, unlike in macroscopic nonlinear optics, the local optical susceptibility $\chi^{(n)}(\vec{r}_s)$ depends on the site symmetry about position r_s within the unit cell of the crystal, and, thus, even order nonlinearities can arise due to local inversion symmetry breaking in centrosymmetric materials, for $\vec{G} \neq 0$.

APPENDIX D: WAVE-MIXING SENSITIVITY IN THE SILICON STRUCTURE

Silicon is isostructural with diamond, sharing the same high-symmetry $m\bar{3}m(O_h)$ centrosymmetric point group and Fd$\bar{3}$m space group. There are eight atoms per conventional face-center-cubic unit cell occupying the (8a) tetrahedral sites with $\bar{4}3m(T_d)$ symmetry. A portion of the structure showing the local coordination is shown in Fig. 7. Here, the tetrahedral atomic sites are shown in red, and the covalent bonds are shown schematically in green. Halfway between each bonds are centers of symmetry corresponding to the 16c Wyckoff sites with $\bar{3}m(D_{3d})$ site symmetry; while a general position along the bonds corresponds to the 32e Wyckoff sites with $3m(C_{3v})$ site symmetry. While the overall structure has inversion symmetry, clearly
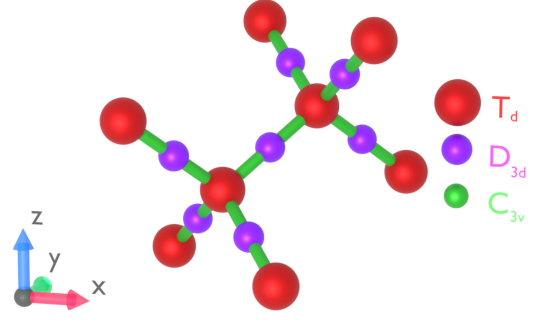

FIG. 7. An illustration of the high-symmetry sites along the tetrahedral bonds for silicon. The red spheres represent the atomic positions at the 8a Wyckoff positions with T_d symmetry, the purple spheres represent the 16c Wyckoff positions at the center of each bond with D_{3d} symmetry, and the green represents the 32e Wyckoff positions with C_{3v} symmetry.

both the atomic sites and the general positions along the bond lack local inversion symmetry about their respective sites.

Note that for the diamond structure $|\rho_{hkl}| \neq 0$ for h, k, l odd or $h + k + l = 4m$ for h, k, l all even and m an integer. Assuming point charges at the atomic sites, $|\rho_{hkl}|$ is maximal $(8f/a^3)$ for the $h + k + l = 4m$ case such as 220, as the tetrahedral sites lie completely within the corresponding atomic planes (for suitable choice of origin). As the valence charge distribution is nonspherically distributed about these sites, it gives rise to finite ρ_{hkl} corresponding to certain otherwise forbidden Bragg peaks such as the 222. This allows for weak diffraction from the valence charge density but not, for example, the 002, which is forbidden by glide plane symmetry.

Because of the cubic symmetry of the lattice, the macroscopic linear optical properties are isotropic, and the induced macroscopic polarization follows the applied field. While this is not strictly true for the microscopic linear response, $\rho_{\vec{G}}^{(1)} \propto \vec{G} \cdot \vec{E}$ for certain $\vec{G}$ along high-symmetry directions (e.g., the 111 and 220). In contrast, the local nonlinear optical response can be anisotropic, even along these high-symmetry directions. Thus, the symmetry of the second-order response can be used to help localize the induced charges even without direct phase information.

The form of $\chi_{(\vec{G})}^{(n)}$ and, thus, $\Gamma_{\vec{G}}^{(n)}$ depends on the local symmetries of $\chi^{(n)}(\vec{r})$ and the particular $\vec{G}$. It can easily be seen that $\Gamma_{hkl}^{(2)} = 0$ for the tetrahedral sites, when $h + k + l = 4m$, even though locally these sites break inversion symmetry. This is due to the overall inversion symmetry of the point group that requires $\chi^{(2)}(\vec{r}) = -\chi^{(2)}(-\vec{r})$ such that the second-order dipoles at the tetrahedral sites are 180° out of phase in every other plane. Thus, by an analysis of the second-order sidebands from the 220 reflection, we can localize the induced charge away from the tetrahedral sites by its site symmetry.

APPENDIX E: ISOLATION OF FOURIER COMPONENTS

In the experiments, we make use of phase matching in combination with an energy-resolving analyzer to isolate particular spatial and temporal Fourier component of the induced density. Although the optical wave vector is approximately $10\,000$ times smaller than the x-ray wave vector, it plays an important role in the phase-matching condition. In general, phase matching implies satisfying crystal momentum and energy conservation:

$$\vec{k}^{(n)} - \vec{k}_x = n\vec{k}_o + \vec{G} \equiv \vec{Q}^{(n)} \quad \text{and} \tag{E1}$$

$$\omega^{(n)} = \omega_x + n\omega_o, \tag{E2}$$

where $\vec{k}_o$, $\vec{k}_x$, and $\vec{k}^{(n)}$ are the optical, incident x-ray, and nonlinear diffracted x-ray wave vectors, respectively, inside the material. The angle between the incident and diffracted x-rays, θ_s satisfies

$$\cos\theta_s \equiv \hat{k}_x \cdot \hat{k}^{(n)} = \frac{(k^{(n)})^2 + k_x^2 - (Q^{(n)})^2}{2k_x k^{(n)}}. \tag{E3}$$

While the angle between the incident x-rays and the lattice planes,

$$\theta = \sin^{-1}\left(\frac{Q^{(n)}\sin\theta_{Q^{(n)}}}{\sqrt{(G+k_{o\parallel})^2 + k_o^2 - k_{o\perp}^2}}\right) + \frac{n}{|n|}\tan^{-1}\left(\frac{k_{o\parallel}}{G+k_{o\parallel}}\right), \tag{E4}$$

where $k_{o\parallel}$ and $k_{o\perp}$ are the components of $\vec{k}_o$ within and perpendicular to the plane containing $\vec{G}$ and $\vec{k}_x$, respectively.

$$\sin\theta_Q \equiv -\hat{k}_x \cdot \hat{Q}^{(n)} = \frac{(Q^{(n)})^2 - (k^{(n)})^2 + k_x^2}{2k_x Q^{(n)}} \tag{E5}$$

is the sine of the angle the incident x-rays make relative to the planes perpendicular to $\vec{Q}^{(n)}$.

Since $\omega_o \ll \omega_x$, $k_o \ll k_x$, to first order in the ratio $x = \omega_o/\omega_x$, the deviation of the input angle relative to the Bragg angle θ_B is

$$\Delta\theta \equiv \theta - \theta_B \tag{E6}$$

$$= \frac{nx}{\sin 2\theta_B}(n_o(\cos\beta\cos\theta_G - \sin\alpha\sin\theta_B) - 1), \tag{E7}$$

where n_o is the index of refraction of the optical beam. α is the angle that the internal optical beam makes relative to the

lattice planes, and γ is the angle that the optical beam makes perpendicular to the plane containing $\vec{k}$ and $\vec{G}$ (note that $\cos^2\beta = \cos^2\alpha - \sin^2\gamma$). We have neglected the small difference in the x-ray index from unity. If $\vec{k}_o$ is also largely in plane, such that $\alpha \approx \beta$,

$$\Delta\theta = \frac{nx}{\sin 2\theta_B}(n_o\cos(\theta_B + \alpha) - 1). \tag{E8}$$

Note that the deviation of the scattering angle from $2\theta_B$,

$$\Delta\theta_s \equiv \theta_s - 2\theta_B \tag{E9}$$

$$\approx -\frac{nx}{\cos\theta_B}(n_o\sin\alpha + \sin\theta_B), \tag{E10}$$

independent of γ. Since $x \ll 1$, $\Delta\theta, \Delta\theta_s \ll 1$, the difference between the exact solution and the first-order approximation is negligible. Nonetheless, since the induced density is a small fraction of the total density, we rely on the finite deviations to isolate the mixing signal. This imposes stringent requirements on the monochromation and collimation of the incident beam as well as the background rejection that includes rejecting the tails of the elastic Bragg peak. This is true even for measurements of wave mixing in nominally perfect crystals such as diamond and silicon. As described in Sec. II, we achieve this by using a matched pair of Si (311) channel-cut crystals in a dispersive geometry for both the monochromator and analyzer.

---

[1] N. W. Ashcroft and N. D. Mermin, *Solid State Physics* (Holt-Saunders, New York, 1976).

[2] R. M. Martin, *Lattice vibrations in silicon: Microscopic dielectric model*, Phys. Rev. Lett. **21**, 536 (1968).

[3] R. M. Martin, *Dielectric screening model for lattice vibrations of diamond-structure crystals*, Phys. Rev. **186**, 871 (1969).

[4] R. W. James, *The Optical Principles of the Diffraction of X-rays* (G. Bell, London, 1948) (original edition).

[5] J. B. Roberto, B. W. Batterman, and D. T. Keating, *Diffraction studies of the (222) reflection in Ge and Si: Anharmonicity and the bonding electron*, Phys. Rev. B **9**, 2590 (1974).

[6] J. Hastings and B. Batterman, *High-order anharmonic forbidden neutron reflections in silicon*, Phys. Rev. B **12**, 5580 (1975).

[7] Y. Yang and P. Coppens, *On the experimental electron distribution in silicon*, Solid State Commun. **15**, 1555 (1974).

[8] Z. W. Lu, A. Zunger, and M. Deutsch, *Electronic charge distribution in crystalline diamond, silicon, and germanium*, Phys. Rev. B **47**, 9385 (1993).

[9] I. Freund and B. Levine, *Optically modulated x-ray diffraction*, Phys. Rev. Lett. **25**, 1241 (1970).

[10] P. Eisenberger and S. McCall, *Mixing of x-ray and optical photons*, Phys. Rev. A **3**, 1145 (1971).

[11] T. E. Glover, D. Fritz, M. Cammarata, T. Allison, S. Coh, J. Feldkamp, H. Lemke, D. Zhu, Y. Feng, R. Coffee *et al.*, *X-ray and optical wave mixing*, Nature (London) **488,** 603 (2012).

[12] D. Popova-Gorelova, D. A. Reis, and R. Santra, *Theory of x-ray scattering from laser-driven electronic systems*, Phys. Rev. B **98,** 224302 (2018).

[13] D. Popova-Gorelova and R. Santra, *Atomic-scale imaging of laser-driven electron dynamics in solids*, Commun. Phys. **7,** 317 (2024).

[14] C. Boemer, D. Krebs, A. Benediktovitch, E. Rossi, S. Huotari, and N. Rohringer, *Towards novel probes for valence charges via x-ray optical wave mixing*, Faraday Discuss. **228,** 451 (2021).

[15] D. Krebs and N. Rohringer, *Theory of parametric x-ray optical wavemixing processes*, arXiv:2104.05838.

[16] K. Tamasaku, K. Sawada, E. Nishibori, and T. Ishikawa, *Visualizing the local optical response to extreme-ultraviolet radiation with a resolution of $\lambda/380$*, Nat. Phys. **7,** 705 (2011).

[17] A. Schori, C. Bömer, D. Borodin, S. P. Collins, B. Detlefs, M. Moretti Sala, S. Yudovich, and S. Shwartz, *Parametric down-conversion of x rays into the optical regime*, Phys. Rev. Lett. **119,** 253902 (2017).

[18] S. Sofer, O. Sefi, E. Strizhevsky, H. Aknin, S. P. Collins, G. Nisbet, B. Detlefs, C. J. Sahle, and S. Shwartz, *Observation of strong nonlinear interactions in parametric down-conversion of x-rays into ultraviolet radiation*, Nat. Commun. **10,** 5673 (2019).

[19] J. D. Jackson, *Classical Electrodynamics* (John Wiley & Sons, New York, 1998).

[20] M. Chollet, R. Alonso-Mori, M. Cammarata, D. Damiani, J. Defever, J. T. Delor, Y. Feng, J. M. Glownia, J. B. Langton, S. Nelson *et al.*, *The x-ray pump-probe instrument at the linac coherent light source*, Synchrotron Radiat. News **22,** 503 (2015).

[21] N. Hartmann, W. Helml, A. Galler, M. R. Bionta, J. Grünert, S. L. Molodtsov, K. Ferguson, S. Schorb, M. Swiggers, S. Carron *et al.*, *Sub-femtosecond precision measurement of relative x-ray arrival time for free-electron lasers*, Nat. Photonics **8,** 706 (2014).

[22] K. Momma and F. Izumi, VESTA3 *for three-dimensional visualization of crystal, volumetric and morphology data*, J. Appl. Crystallogr. **44,** 1272 (2011).

[23] G. Bricogne, *Maximum entropy and the foundations of direct methods*, Found. Crystallogr. **40,** 410 (1984).

[24] E. Weckert and K. Hümmer, *Multiple-beam x-ray diffraction for physical determination of reflection phases and its applications*, Found. Crystallogr. **53,** 108 (1997).

[25] S. Ghimire and D. A. Reis, *High-harmonic generation from solids*, Nat. Phys. **15,** 10 (2019).

[26] D. Basov, R. Averitt, and D. Hsieh, *Towards properties on demand in quantum materials*, Nat. Mater. **16,** 1077 (2017).

[27] S. Huang, Y. Ding, Y. Feng, E. Hemsing, Z. Huang, J. Krzywinski, A. A. Lutman, A. Marinelli, T. J. Maxwell, and D. Zhu, *Generating single-spike hard x-ray pulses with nonlinear bunch compression in free-electron lasers*, Phys. Rev. Lett. **119,** 154801 (2017).

[28] J. Yan, W. Qin, Y. Chen, W. Decking, P. Dijkstal, M. Guetg, I. Inoue, N. Kujala, S. Liu, T. Long, N. Mirian, and G. Geloni, *Terawatt-attosecond hard x-ray free-electron laser at high repetition rate*, Nat. Photonics **18,** 1293 (2024).

[29] D. Zhu and D. A. Reis, *Attosecond x-ray laser vision*, Nat. Photonics **18,** 1232 (2024).

[30] D. Popova-Gorelova and R. Santra, *Microscopic nonlinear optical response: Analysis and calculations with the Floquet-Bloch formalism*, Struct. Dyn. **11,** 014102 (2024).

[31] Z. H. Levine and D. C. Allan, *Linear optical response in silicon and germanium including self-energy effects*, Phys. Rev. Lett. **63,** 1719 (1989).

[32] J. Phillips, *Band structure of silicon, germanium, and related semiconductors*, Phys. Rev. **125,** 1931 (1962).

[33] M. S. Hybertsen and S. G. Louie, *First-principles theory of quasiparticles: Calculation of band gaps in semiconductors and insulators*, Phys. Rev. Lett. **55,** 1418 (1985).

[34] B. E. Warren, *X-Ray Diffraction* (Courier Corporation, New York, 1990).